Nano Energy 36 (2017) 46–57

Contents lists available at ScienceDirect

Nano Energy

journal homepage: www.elsevier.com/locate/nanoen

Full paper

Toward ultrafast lithium ion capacitors: A novel atomic layer deposition seeded preparation of $Li_4Ti_5O_{12}$/graphene anode

Gongkai Wang[a,**], Chengxing Lu[a,b], Xin Zhang[a], Biao Wan[c], Hanyu Liu[d], Meirong Xia[e], Huiyang Gou[c,e,*], Guoqing Xin[f], Jie Lian[f,*], Yongguang Zhang[a]

[a] *Research Institute for Energy Equipment Materials, Tianjin Key Laboratory of Materials Laminating Fabrication and Interface Control Technology, Hebei University of Technology, Tianjin 300130, China*
[b] *School of Material Science & Engineering, Hebei University of Technology, Tianjin 300130, China*
[c] *Center for High Pressure Science and Technology Advanced Research, Beijing 100094, China*
[d] *Geophysical Laboratory, Carnegie Institution of Washington, 5251 Broad Branch Road NW, Washington, DC 20015, USA*
[e] *Key Laboratory of Applied Chemistry, College of Environmental and Chemical Engineering, Yanshan University, Qinhuangdao 066004, China*
[f] *Department of Mechanical, Aerospace, and Nuclear Engineering, Rensselaer Polytechnic Institute, Troy, New York 12180-3590, USA*

ARTICLE INFO

Keywords:
$Li_4Ti_5O_{12}$/graphene
Atomic layer deposition
Seeded route
Anode
Lithium ion capacitor

ABSTRACT

High performance composite of nanosized $Li_4Ti_5O_{12}$ (LTO) and graphene nanosheets was fabricated using a novel atomic layer deposition (ALD) seeded process incorporated with hydrothermal lithiation for the first time. TiO_2 nanoislands as seeds were anchored on graphene by ALD process, triggering the unique structure formation of subsequent LTO. The synergistic effects of nanosized LTO and graphene endow the composite with a short lithium ion diffusion path and efficiently conductive network for electron and ion transport, boosting the excellent reversible capacity, rate capability, and cyclic stability as anode materials for lithium ion capacitors (LICs). The reversible capacity of 120.8 mA h g^{-1} at an extremely high current rate of 100 C was achieved successfully, and the electrode can be charged/discharged to about 70% of the theoretical capacity of LTO in 25 s. Meanwhile, the composite exhibited excellent cyclic stability of 90% capacity retention at 20 C with nearly 100% Coulombic efficiency after 2500 cycles. The sintering treatment after hydrothermal reaction has significant effects on the crystallinity, defect density, microstructure and electrochemical property of the composite, which is also supported by theoretical calculations. The results provide a versatile roadmap for synthesis of high performance LTO based composite and new insights into LICs.

1. Introduction

The ever-increasing global energy-consumption because of the planetary climate change, disastrous environmental pollution and substantial deficit of fossil fuels requires the development of advanced electrical energy storage technology (EES) [1–3]. Great progress has been made in the development of EES devices such as lithium ion batteries (LIBs) and supercapacitors (SCs) based on electrode material design and cell system optimization [4–7]. As the primary EES unit in the market, LIB could store a large number of charges in the cell; however, they will take several hours to complete the kinetics limited charge/discharge process (due to their low power density). By contrast, SCs could ensure fast energy storage in seconds or minutes, but low energy density limits their vast applications [3,8]. Therefore, next generation of EES devices with intrinsically-improved energy and power densities are highly desirable to meet the requirements of modern technologies. Lithium ion capacitors (LICs) are mainly configurated by LIBs-type anode and SCs-type cathode, which are operated by combined mechanisms of lithium ion intercalation/deintercalation and anion double-layer adsorption/desorption. Therefore, the intriguing combination boosts the energy/power densities simultaneously as compared with the symmetric cell, bridging the gap between LIBs and SCs on the Ragone plot [9–11]. Due to the electrochemical hysteresis, however, the anode performance is the power-output constrain of LICs, which is typically limited by the inherently semi-infinite diffusion process of bulk electrodes, as compared with the surface-controlled charge storage of porous electrodes [12]. This imbalance in kinetics between two electrodes has necessitated the

---

* Corresponding authors.

** Corresponding author at: Research Institute for Energy Equipment Materials, Tianjin Key Laboratory of Materials Laminating Fabrication and Interface Control Technology, Hebei University of Technology, Tianjin 300130, China.

E-mail addresses: wang.gongkai@hebut.edu.cn (G. Wang), huiyang.gou@hpstar.ac.cn (H. Gou), lianj@rpi.edu (J. Lian).

http://dx.doi.org/10.1016/j.nanoen.2017.04.020
Received 23 March 2017; Received in revised form 13 April 2017; Accepted 13 April 2017

anode material with superior rate capability and cyclic stability.

Among a myriad of anode materials, the spinel-structured $Li_4Ti_5O_{12}$ (LTO) has attracted tremendous attention especially in terms of safety issues recently because of the battery incidents such as Samsung Note 7. LTO with a three-dimensional (3D) lithium diffusion structure exhibits the negligible volume change during the lithiation/delithiation. Meanwhile, the relatively flat and high potential plateau around ~1.55 V vs Li^+/Li endows LTO with the excellent cyclic stability and safety. Nevertheless, the intrinsically-poor electronic conductivity (10^{-13}–10^{-8} S cm^{-1}) and lithium ion diffusion kinetics suppress its rate capability [13–15]. Great efforts have been directed towards developing various hierarchically nanostructured LTO or carbonaceous LTO composites to garner maximum power density [16–20]. Unfortunately, several drawbacks in terms of materials design and roadmap selection still exist. Highly porous structured LTO could deliver improved rate capability as compared with the bulk one at expense of tap density and volumetric capacity. High temperature sintering is usually involved in the preparation of LTO powder obtained by solid-state reaction, sol-gel or hydrothermal methods, which is generally accompanied by the grain growth and particle aggregation, hindering the lithium ion diffusion and thus deteriorating the electrochemical performance inevitably. Integrating with carbonaceous components such as amorphous carbon coating, carbon nanotube and graphene could tailor the electrical conductivity of the composite [17,21–25]. As we know, versatile graphene can be served as a building block to improve the performance of active materials [26–29]. Although high quality graphene can be produced massively [30,31], the large-scale application in EES technology has not been reflected so far. That quests for a feasible method with meticulous design to hybridize graphene with active materials rather than just mixing them physically.

ALD has been explored as an important vapor deposition technique in contrast to solution based processes. Semiconductor processing is one of the main motivations for the development of ALD. The ALD process is capable of producing conformal thin films with precise control even at the angstrom scale with excellent uniformity on various host materials including complex 3D substrates, two dimensional (2D) sheets and one dimensional (1D) wires. It is predicted that hierarchical electrode materials and composites could be prepared by ALD, which will open up another novel pathway for applications in EES [32–34].

In this study, ALD technique as an ingeniously seeded route was adopted to obtain high performance composites of nanosized LTO and graphene nanosheets as anode materials for LICs. To the best of our knowledge, this is the first report on synthesis of LTO/graphene composite by an ALD seeded route combined with hydrothermal lithiation. TiO_2 nanoislands were seeded on graphene by ALD process in advance, ensuring the unique structure formation of subsequent LTO. The synergistic effects of nanosized LTO and graphene conductive host defined by ALD boosted excellent rate capability. The reversible capacity of 120.8 mA h g^{-1} at an extremely high current rate of 100 C was achieved, which means that the electrode could be charged/discharged to about 70% of the theoretical capacity of LTO in 25 s. Meanwhile, the composite exhibited good cyclic stability of 90% capacity retention at 20 C with nearly 100% Coulombic efficiency after 2500 cycles. Additionally, the restricting factors in our experiment conditions including synthesis parameters, morphology, microstructure and the corresponding electrochemical kinetics were evaluated systematically. The theoretical calculations revealed the possible origin of high performance of LTO/graphene composite. The present results provide a novel roadmap for synthesis of high performance LTO based composite and new insights into LICs.

2. Experimental section

2.1. Preparation of TiO_2/graphene composite by ALD method

The pristine graphene (Shanghai SIMBATT Energy Technology Co., Ltd, China) synthesized by reduction of graphite oxide (GO) was used as host materials in the ALD process. The ALD seeded process was performed using a rotary reactor (Zhiliande Tech Co. Ltd, Zhenjiang, China). Titanium tetrachloride ($TiCl_4$, 99.8%, Strem Chemicals) and high performance liquid chromatography (HPLC) grade H_2O were employed as precursors. The deposition sequence of ALD TiO_2 was carried out by modified our previous reports [35,36], specifically, the reaction sequence was: (i) $TiCl_4$ dose to 1.0 Torr for 60 s; (ii) evacuation of reaction products and excess $TiCl_4$ for 150 s; (iii) dose N_2 to 20.0 Torr for 200 s and evacuate N_2; (iv) H_2O dose to 1.0 Torr for 60 s; (v) evacuation of reaction products and excess H_2O for 150 s (vi) dose N_2 to 20.0 Torr for 200 s and evacuate N_2. The as-prepared sample was annealed at 120 °C. One complete reaction of $TiCl_4$ and H_2O is defined as one TiO_2 ALD cycle. The typical growth rate for ALD TiO_2 is about 0.6 Å per cycle. The TiO_2/graphene composites were prepared according to 50 and 100 ALD cycles denoted as 50-TiO_2-G and 100-TiO_2-G in our experiment. The as-obtained TiO_2/graphene composite was used directly for the following hydrothermal reaction.

2.2. Preparation of LTO/graphene composite by hydrothermal method

Typically, an appropriate amount of as-prepared TiO_2/graphene composite was added to 2 M LiOH aqueous solution (5 ml) under stirring for 1 h. Subsequently, the suspension was sealed in a 15 ml Teflon-lined autoclave and maintained at 180 °C for 24 h. After the autoclave was naturally cooled to room temperature, the precipitates were collected by centrifuging and washed with deionized water and ethanol. Then the separated precipitates were vacuum dried at 60 °C for 12 h. Finally, the dried precipitates were sintered at 600 °C for 6 h under Ar atmosphere at a ramping rate of 5 °C min^{-1}. The samples based on different TiO_2/graphene composites were labeled as 50-LTO-G-600C and 100-LTO-G-600C, respectively. Different hydrothermal conditions including temperature, duration and Li ion concentration were also performed in our experiment condition. 1 M and 5 M LiOH aqueous solutions were used as reagents following the same process as the control experiment. The hydrothermal conditions such as 120 °C for 24 h, 200 °C for 24 h and 180 °C for 48 h were also performed for the optimization of synthesis. Additionally, the dried precipitates were also sintered at 800 °C denoted as 100-LTO-G-800C in order to claim the effect of sintering temperature on the physical characteristic and electrochemical property of LTO/graphene composite.

2.3. Material characterizations

X-ray diffraction (XRD) analysis was performed using a Bruker D8-focus X-ray powder diffractometer equipped with a Cu Kα radiation (wavelength of 1.542 Å) in the 2θ range between 10° and 90° at room temperature. The Brunauer-Emmett-Teller (BET) surface area of materials was recorded using a Micromeritics ASAP2020 M+C instrument based on the nitrogen adsorption/desorption isotherm at 77 K. X-ray photoelectron spectroscopy (XPS) was carried out on a Thermo Scientific ESCALAB 250XI Probe system. Raman spectra were recorded on aspectrometer (inVia Reflex, Renishaw, UK) with a laser excitation wavelength of 532 nm in the range of 200–2000 cm^{-1}. The morphology and microstructure of materials were characterized by a field emission scanning electron microscope (FESEM, JEOL JSM-7100F) coupled with an energy dispersive X-ray spectrometer (EDS) and a transmission electron microscopy (TEM, Tecnai LaB6). Thermogravimetric analysis (TGA, SDTQ-600, TA Instruments-Waters LLC) was conducted from room temperature to 700 °C in air with a heating rate of 5 °C min^{-1}.

2.4. Electrochemical measurements

The as-obtained LTO/graphene composites (50-LTO-G-600C, 100-

LTO-G-600C and 100-LTO-G-800C) were investigated using coin cells (CR2025). Firstly, the working electrode was prepared by mixing 80 wt% active materials, 10 wt% acetylene black and 10 wt% binder (polyvinylidene difluoride, PVDF) dissolved in N-methylpyrrolidone (NMP). The resultant slurry was uniformly coated onto a copper current collector and vacuumdried at 120 °C for 12 h, and then punched and pressed under a pressure of 24 MPa. The mass loadings of the electrode material are between 1.5 and 2.8 mg cm^{-2}. The coin cells were assembled by using lithium foil as the counter and reference electrodes in an Ar-filled glove box (Mikarouna-MKUS2-1611-0091, China). A Celgrad 2400 microporous polyethylene membrane as separator was sandwiched between anode and cathode. The electrolyte was 1 M $LiPF_6$ in a mixture of ethylene carbonate (EC) and diethyl carbonate (DMC) (1:1 by volume). Cyclic voltammogram (CV) was recorded using an electrochemical workstation (Ametek, Princeton Applied Research, Versa STAT 4) at various scan rates (0.1–10 mV s^{-1}) in a cutoff voltage of 1.0–2.5 V. The electrochemical impedance spectroscopy (EIS) was also measured in the frequency range from 100 kHz to 0.1 Hz. Galvanostatic charge/discharge measurement was performed at different current rates (0.5–100 C, 1 C corresponds to 175 mA g^{-1}) using a multi-channel battery testing system (Neware BTS4000) in the potential range of 1.0–3.0 Vvs. Li^+/Li. The electrochemical performance of pristine graphene was also investigated as a control experiment. The coin cell assembling and electrochemical measurement were followed the process of the LTO/graphene composite. In terms of LICs full cell measurement, activated carbon (AC) (Kuraray Chemical Co., Ltd., YP-50F) was used as cathode material. The corresponding electrochemical performance measurement of AC was followed the same procedure except using aluminum foil as a current collector. The LICs full cell based on 100-LTO-G-600C anode and AC cathode was also assembled in the Ar-filled glove box. The cutoff potentials were set as 3.0–4.5 Vand 1.5–3.0 V vs. Li^+/Li, corresponding to AC cathode and LICs full cell, respectively. All the electrochemical measurements were carried out at room temperature. The specific capacity could be converted into specific capacitance according to the following equation: C_s (F g^{-1}) $=\frac{I\times\Delta t}{3600\times m}=C\,(\mathrm{mA\,h\,g^{-1}})\times\frac{3600}{dV}$, where I (A) is the constant current, Δt (s) is the discharge time, m (g) is the mass of active materials, C (mA h g^{-1}) is the specific capacity and dV (mV) is the potential window [37]. The energy density (E, W h kg^{-1}) and power density (P, W kg^{-1}) of the LICs full cell were calculated according to the equations:$E=\int_{t_1}^{t_2} IVdt=\frac{1}{2}C\,(V_{max}+V_{min})(V_{max}-V_{min})=\Delta V\times\frac{I}{m}\times t,\ P=\frac{E}{t}=\Delta V\times\frac{I}{m}$, $\Delta V=\frac{V_{max}+V_{min}}{2}$, where$V_{max}$ and V_{min} are the initial and final discharge potentials (V) and$m$ is the total mass of active materials in anode and cathode [38].

3. Results and discussion

Aiming to address above issues, there are three main strategies employed in this study as follows: (I) decrease the LTO particle size (II) combine with graphene nanosheets synergistically and (III) reduce the post-sintering temperature. Based upon these, the schematic illustration is shown in Fig. 1, presenting the typical synthesis procedure. The uniform TiO_2 nanoislands as seeds were deposited on graphene nanosheets by ALD process in advance. Then, LTO/graphene composite was prepared by means of hydrothermal lithiation with LiOH aqueous solution followed by sintering at 600 °C. First, the discontinued TiO_2 nanoislands instead of a fully covered film on graphene nanosheets were obtained by the control of ALD process, serving as nucleation sites of lithiation, which is a crucial step of confining the particle size for subsequent LTO. Secondly, the chemical bonding connected graphene with LTO defined by ALD can also facilitate the electron and ion transport and structural stability besides the effect of graphene itself, benefiting for the electrochemical performance of LTO. Meanwhile, the isolation of TiO_2 nanoisland avoided the particle aggregation of LTO during following sintering process, ensuring the analogously topological transformation from TiO_2 to LTO on graphene. Thirdly, the involved hydrothermal lithiation could decrease the post-sintering temperature of the formation of LTO phase efficiently, hindering grain growth, reducing high degree of crystallinity, and thus leading to the improved performance of LTO as well.

The growth mechanism of ALD TiO_2 is proposed following the reaction (A) and (B) below:

(A) n(-OH)+$TiCl_4$ – > (-O-)$_n$$TiCl_{4-n}$+$n$HCl

(B) (-O-)$_n$$TiCl_{4-n}$+(4-$n$)$H_2O$ – > (-O-)$_n$$Ti(OH)_{4-n}$+(4-$n$) HCl

TiO_2 could be obtained after low temperature annealing of TiOH species on graphene. Reactions (A) and (B) were defined as one ALD cycle. The TiO_2/graphene composite was prepared according to 50 and 100 ALD cycles denoted as 50-TiO_2-G and 100-TiO_2-G in our experiment. Fig. 2a shows X-ray diffraction (XRD) patterns of the TiO_2/graphene composite. Both composites exhibited a main diffraction peak located around 25° and some small peaks, which can be indexed to anatase TiO_2 (JCPDS no. 21-1272). The main peak of 100-TiO_2-G becomes sharper than that of 50-TiO_2-G, indicating the growth of crystal size with increased ALD cycles. The crystal sizes of 50-TiO_2-G and 100-TiO_2-G are ~8.5 and ~10 nm, respectively, calculated by Scherrer equation based on the (101) plane of TiO_2.

The porous microstructure of the TiO_2/graphene composite was evaluated by nitrogen adsorption/desorption isotherms as shown in Fig. 2b. The composite exhibited the typical Type IV isotherm with Type H3 hysteresis loop, suggesting the hierarchical pore structure associated with meso- and macropores [39]. The open pore structure facilitates the solvent transport during the following hydrothermal reaction, determining the unique structure formation of subsequent LTO. The suggestion was in accordance with the pore size distribution (the inset in Fig. 2b). The composite presented small size mesopores (about 3–4 nm) with a broad macropores distribution. The calculated specific surface areas of 50-TiO_2-G and 100-TiO_2-G are 195.4 and 159.4 m^2 g^{-1}, respectively. The corresponding TiO_2 contents of 54.4% and 64.8% were determined by Thermogravimetric analysis (TGA) (Fig. S1, Supporting information). Fig. S2 shows a X-ray photoelectron spectroscopy (XPS) spectrum identifying the surface valence state of elements in 100-TiO_2-G, which agrees well with the previous reports [35,36]. It is worthy of note that the chemical bonding between TiO_2 and graphene defined by ALD may improve the electron transport and structural stability as well.

The morphology of the TiO_2/graphene composite was observed by scanning electron microscopy (SEM) (Fig. 2c, d) and transmission electron microscopy (TEM) (Fig. 2e, f). TiO_2 nanoislands with the average size of 20 nm were distributed uniformly on the wrinkled graphene nanosheets. Instead of a fully covered TiO_2 film on graphene, discontinued nanoisland structure was inclined to form. On one hand, the hydroxyl-covered surface of 2D graphene controlled by ALD process induced the interaction with $TiCl_4$ molecules. On the other hand, TiO_2 nucleated and growed at the defect sites (or residually functional groups after oxidation-reduction synthesis) on graphene due to the nucleation difficulty on π-state sp^2 carbon network, which also determined the formation of nanoisland morphology [35,36,40]. More importantly, the isolated TiO_2 nanoisland is the prerequisite for confining subsequent LTO nanoparticles. The inter-planar spacing of 0.35 nm corresponded to the (101) plane of anatase TiO_2 (Fig. 2f), which is consistent with the XRD result.

After ALD seeded process, LTO/graphene composite was synthesized by the hydrothermal reaction based on LiOH aqueous solution and as-prepared 50-TiO_2-G and 100-TiO_2-G followed by post-sintering at 600 °C. The samples were labeled as 50-LTO-G-600C and 100-LTO-G-600C. The corresponding XRD patterns were depicted in Fig. 3a. The well matched diffraction peaks can be assigned to the spinel structured LTO (JCPDS No. 49–0207). The broad "hump" around 26° was

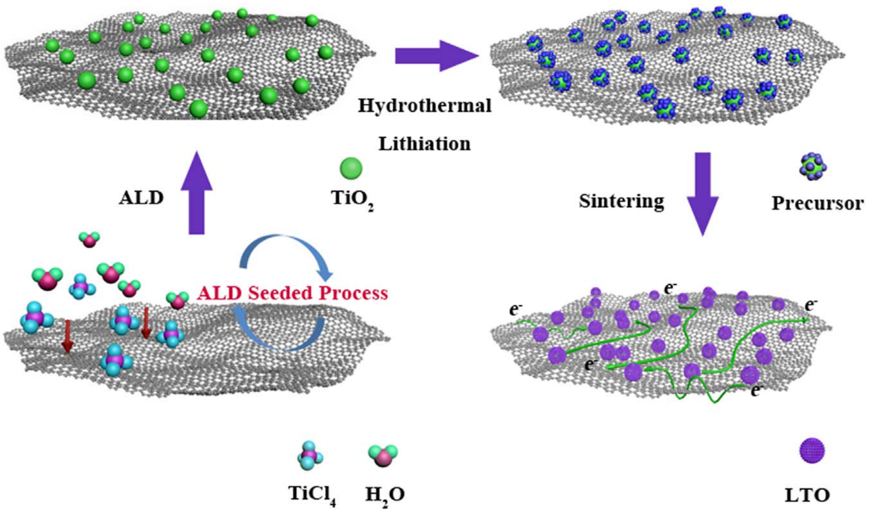

Fig. 1. Schematic illustration of a typical ALD seeded process incorporated with hydrothermal lithiation and the as-obtained LTO/graphene composite.

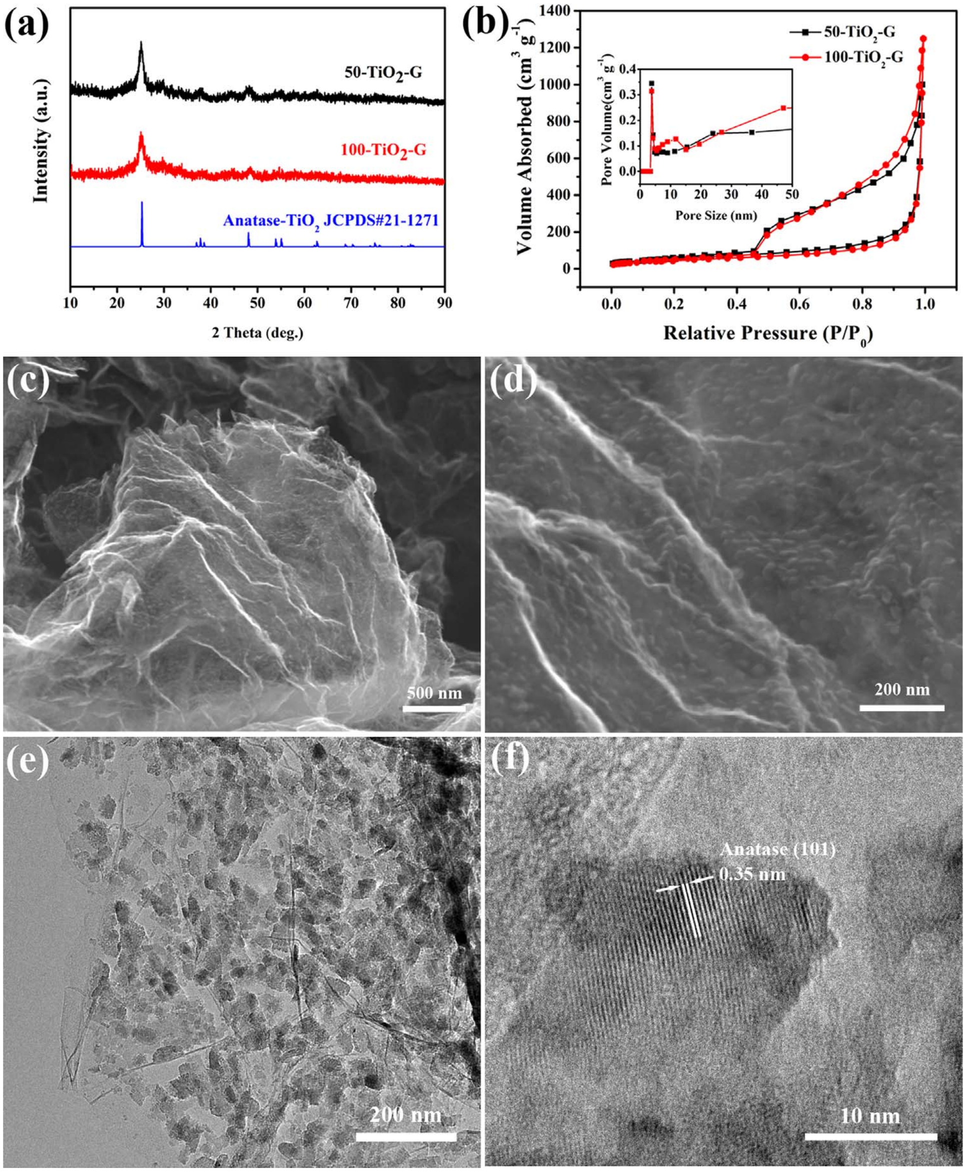

Fig. 2. (a) XRD patterns of 50-TiO_2-G and 100-TiO_2-G, (b) Nitrogen adsorption/desorption isotherms and (inset) the corresponding pore size distribution of the TiO_2/graphene composites, (c, d) SEM and (e, f) TEM images of the TiO_2/graphene composites.

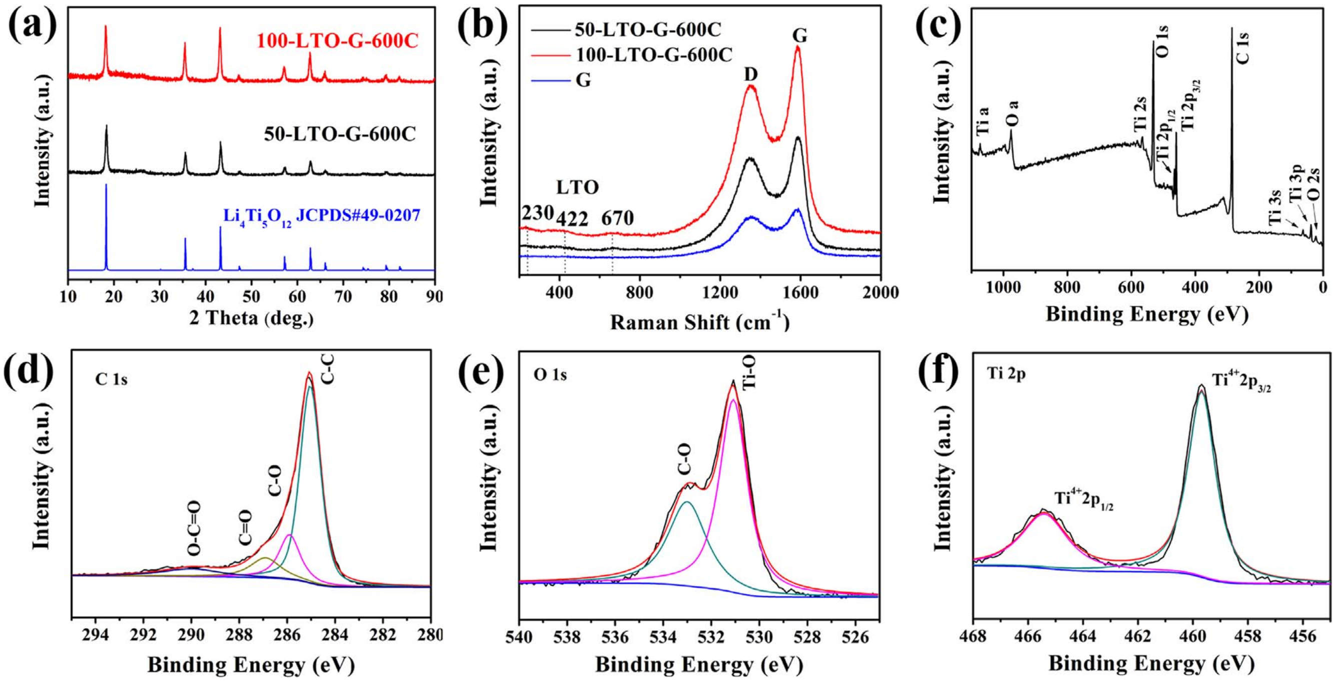

Fig. 3. XRD patterns of 50-LTO-G-600C and 100-LTO-G-600C, (b) Raman spectra of the LTO/graphene composite and pristine graphene, XPS of the LTO/graphene composite (c) Survey, (d) C 1s, (e) O 1s and (f) Ti 2p.

associated with the disordered layer stacking of graphene nanosheets. No impurities (such as TiO_2 and Li_2TiO_3) were observed, demonstrating the formation of pure LTO phase after appropriate hydrothermal lithiation and sintering at 600 °C. The effects of hydrothermal temperature, duration and Li ion concentration on the pure LTO phase formation were investigated in our experiment condition. Fig. S3 shows the XRD patterns of samples obtained under various hydrothermal temperatures and durations with 1 M LiOH at 800 °C. The patterns unequivocally revealed that there was no identified LTO phase formation until the hydrothermal temperature rose up to 180 °C. Meanwhile, there were still impure phases by even further increasing the temperature and duration. Fig. S4 shows the XRD patterns of samples prepared under different Li ion concentrations treated by hydrothermal temperature of 180 °C for 24 h at 800 °C. The results indicated that over high Li ion concentration (5 M) induced Li_2TiO_3 impurity. Additionally, the pure LTO phase can also be obtained at 600 °C sintering (Fig. 3a). Therefore, the synthesis conditions of the LTO/graphene composite were optimized according to a series of experiments in this work. The LTO mass percentages of 80.6% and 92.4% were contained corresponding to 50-LTO-G-600C and 100-LTO-G-600C, respectively (Fig. S5).

The molecule state of composite and pristine graphene nanosheets was also identified by Raman spectroscopy (Fig. 3b). In the spectra, three broad peaks at 100–800 cm^{-1} were observed. The peak at 235 cm^{-1} was attributed to the vibration of O-Ti-O counterpart. The stretching-bending vibration of the Li-O bond in LiO_4 and LiO_6 polyhedra usually induces the characteristic peak at about 430 cm^{-1}. The peak at about 675 cm^{-1} was assigned to the vibration of the Ti-O bond in TiO_6 octahedra [41,42]. The D- and G-bands (corresponding to the in-phase vibration of graphite lattice and disordered or defected graphite) located at ~1350 cm^{-1} and 1580 cm^{-1}, respectively, were ascribed to grapheme [29,43], suggesting the characteristic of graphene with remained defects that would be the nucleation sites of TiO_2 during the ALD process. No other characteristic peaks could be observed in the spectra, indicating a pure LTO phase without any impurities.

Similarly, the surface valence state of elements in the LTO/graphene composite (100-LTO-G-600C) was conducted by XPS. The survey spectrum shows three major peaks located at around 284.5, 531.1 and 459.8 eV, which are indexed to the characteristic peaks of C1s, O1s and Ti2p, respectively (Fig. 3c). The corresponding high resolution XPS spectrum was analyzed. The C1s spectrum presents a prominent peak (C-C) with some merged peaks (C-O and C=O) [44], associated with graphene sp^2 domains and residually oxygen-containing functional groups, respectively (Fig. 3d). Fig. 3e clearly shows a C-O bond at 532.9 eV besides the Ti-O bond, implying the chemical bonding between LTO and graphene throughout the composite. This kind of synergistic integration facilitates the electron and ion transport during the electrochemical charge/discharge process. The spin orbit splitting of Ti2p with the peak separation of 5.8 eV is observed in Fig. 3f, indicating the presence of normal state of Ti^{4+} [45].

The nitrogen adsorption/desorption isotherms and microscopy were also employed to provide further information for the LTO/graphene composites with respect to the microstructure and morphology. The composite exhibited analogous features about porosity as compared with that of TiO_2/graphene. The typical Type IV isotherm with Type H3 hysteresis loop was observed (Fig. 4a), indicating the hierarchical pore structure. The smaller hysteresis loop of 100-LTO-G-600C was observed due to the increased mass of LTO than that of 50-LTO-G-600C. The composite showed the similar pore size distribution of small size mesopores around 3.8 nm and macropores except the decreased pore volume of 100-LTO-G-600C (Fig. 4b). The calculated specific surface areas of 50-LTO-G-600C and 100-LTO-G-600C are 142.6 and 126.3 $m^2 g^{-1}$, respectively, demonstrating nearly undisturbed porosity with relatively high surface area in contrast to TiO_2/graphene even after the hydrothermal reaction. The appropriate porosity and surface area play a pivotal role in outputting superior electrochemical performance. Additionally, the nitrogen adsorption/desorption isotherm and pore size distribution of pristine graphene was also provided in Fig. S6. The calculated specific surface area was about 674 $m^2 g^{-1}$. The hierarchical feature of porosity with meso- and macropores was identified. Therefore, this combined ALD and hydrothermal approach is believed to synthesize extensive composites based on even more complicated structured host materials with nearly negligible effects on the original structure of host materials.

As shown in SEM images (Fig. 4c, d), the homogeneous LTO nanoparticles were anchored on the surface of wrinkled graphene

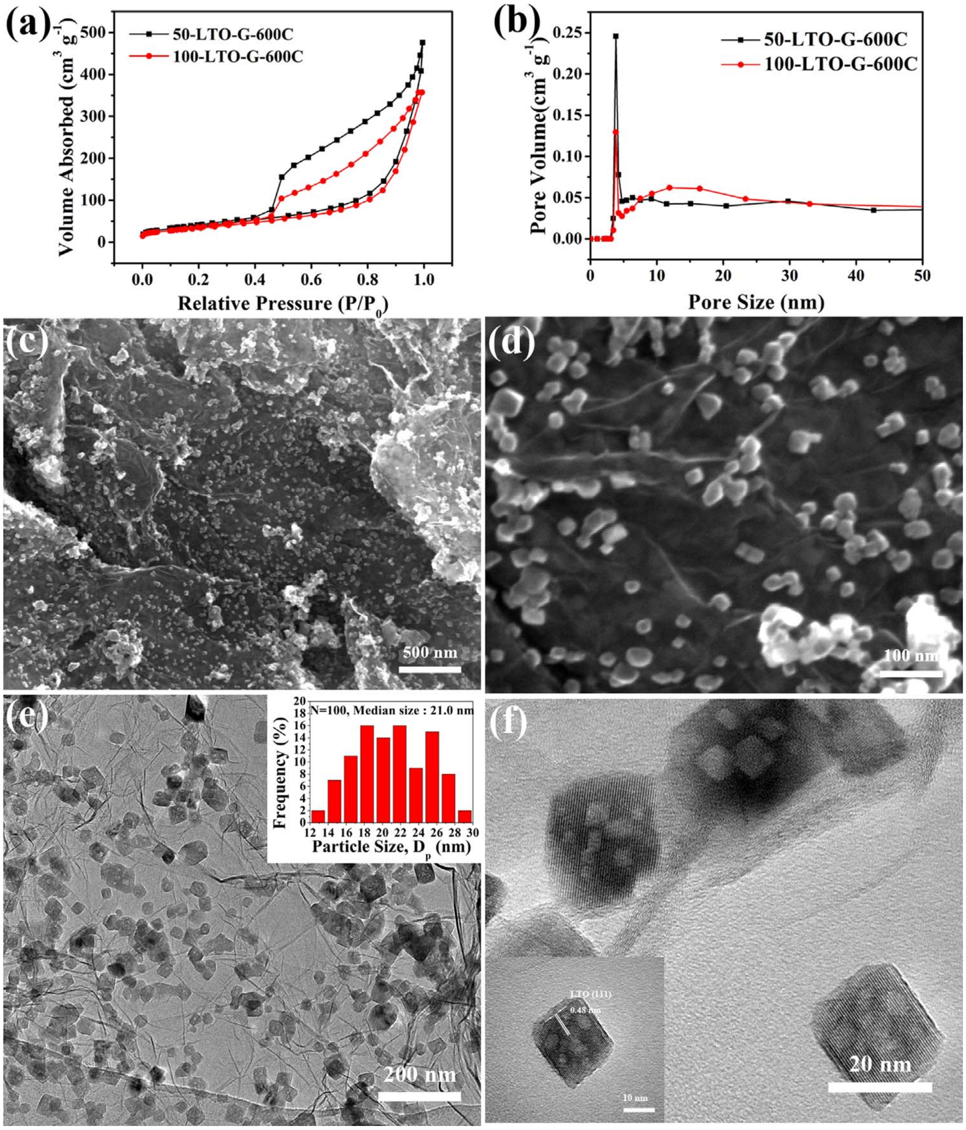

Fig. 4. (a) Nitrogen adsorption/desorption isotherms of 50-LTO-G-600C and 100-LTO-G-600C, (b) corresponding pore size distribution of the LTO/graphene composites, (c, d) SEM images of 100-LTO-G-600C, (e) a TEM image of 100-LTO-G-600C and (inset) the corresponding particle diameter distribution of LTO, and (f) high resolution TEM images of the LTO nanoparticles.

without obvious self-aggregation. As we preconceive, LTO nucleated and grew at the sites of TiO_2 seeds during the hydrothermal reaction. The particle size and distribution of LTO were well confined by ALD TiO_2 seeds which ensured the analogously topological transformation from TiO_2 to LTO. TEM observations provided more insight into morphology and inner structure (Fig. 4e, f). Graphene nanosheets exhibited the randomly crumpled structure with low contrast, indicating few layers with high quality. The isolated LTO nanoparticles were observed clearly on graphene. The calculated particle diameter distribution shows the average size of 100-LTO-G-600C of ~21 nm, revealing a narrow diameter distribution defined by ALD and hydrothermal reaction. The well crystallized LTO particles with lump-sugar like shape are also observed in high resolution TEM. Furthermore, the rough surface observed here may be ascribed to the original structure of TiO_2 nanoisland which grew layer by layer defined by ALD mechanism. The inset in Fig. 4f shows that the LTO particle exhibits a lattice fringe with the inter-planar spacing of 0.48 nm, corresponding to the (111) plane of spinel structured LTO, which is consistent with the XRD result.

Through this ALD seeded route incorporated with hydrothermal and post sintering, the LTO/graphene composite with unique features was obtained. The expected electrochemical properties were evaluated in lithium ion half cells. Fig. 5a, b show the charge/discharge potential profiles of 50-LTO-G-600C and 100-LTO-G-600C measured by galvanostatic charge/discharge at various current rates from 0.5 to 100 C (1 C corresponds to 175 mA g^{-1}) in the voltage range of 1.0–3.0 V vs Li^+/Li. A very flat plateau with two sloping voltage curves (at 3.0–1.5 V and 1.5–1.0 V vs Li^+/Li) was observed with respect to both samples. The flat plateau at about 1.55 V mainly contributed to the total capacity, demonstrating the inherent feature of a two-phase lithiation/delithiation mechanism ($Li_4Ti_5O_{12}$ and $Li_7Ti_5O_{12}$) [46]. At the current rate of 0.5 C, 50-LTO-G-600C and 100-LTO-G-600C could deliver stable specific capacities as high as 212.9 and 209.4 mA h g^{-1}, respectively. The capacity over the theoretical value (175 mA h g^{-1}) of LTO was ascribed to the contributions from graphene host material at early charge/discharge process (reaction between graphene and electrolyte to store lithium ion and form solid electrolyte interphase (SEI)). The first five potential curves at 0.5 C were also presented in Fig. S7. It is worthy of note that the large discharge capacities of 350.1 and 325.5 mA h g^{-1} were achieved at the initial cycle, corresponding to 50-LTO-G-600C and 100-LTO-G-600C, respectively. The long sloping region declined abruptly in the subsequent cycle, which is mainly

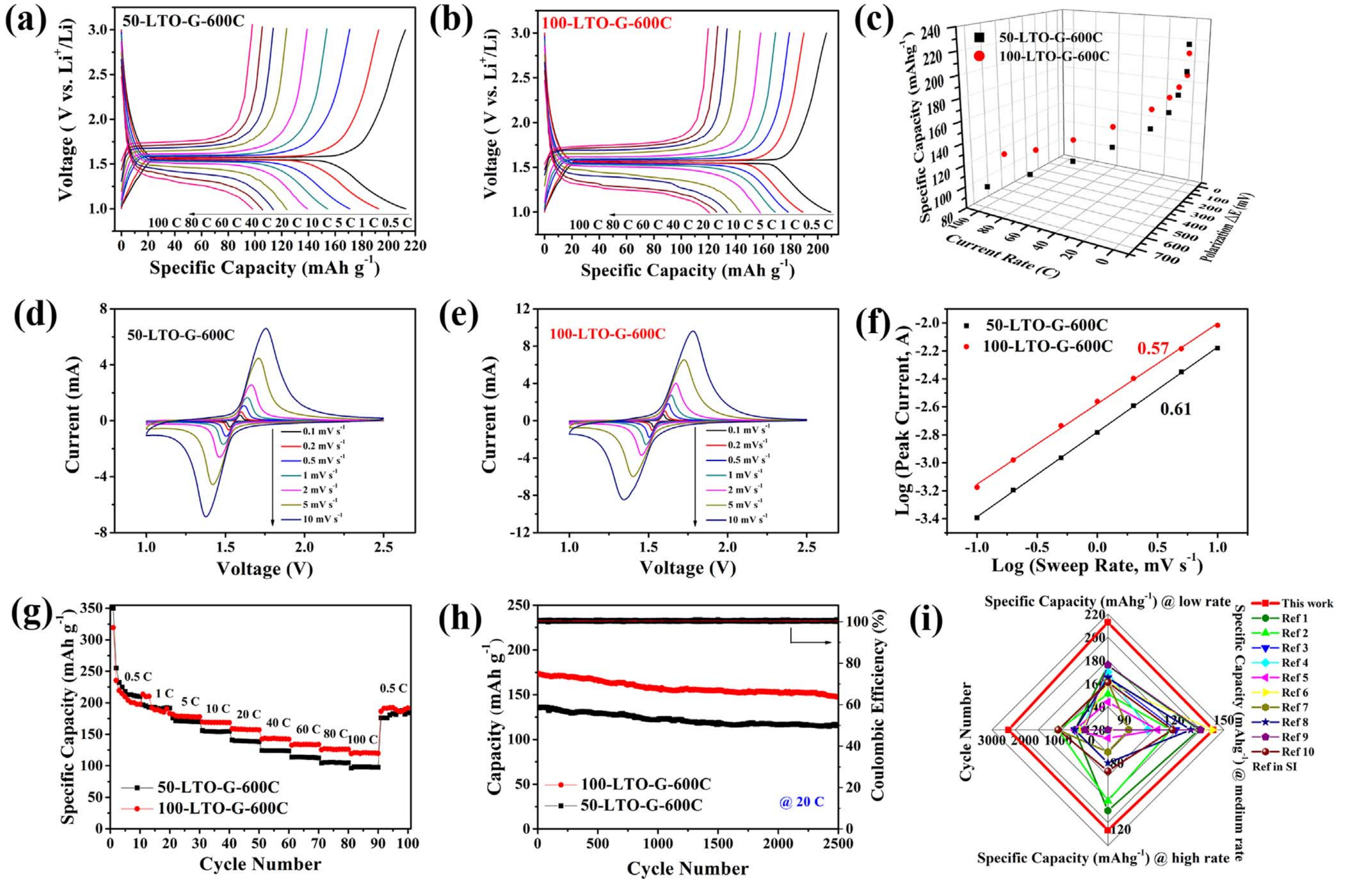

Fig. 5. Charge/discharge potential profiles of (a) 50-LTO-G-600C and (b) 100-LTO-G-600C, (c) relationship of current rate, specific capacity and potential polarization of the LTO/graphene composites, CV curves of (d) 50-LTO-G-600C and (e) 100-LTO-G-600C, (f) dependence of Log (sweep rate) on Log (peak current), (g) cycling rate performance and (h) cyclic stability of the LTO/graphene composites, and (i) comparison of rate capability under various rates and cyclic stability of 100-LTO-G-600C with previous reports.

related to the formation of SEI (upon the reaction between graphene and electrolyte). The following cycles became similar gradually, indicating the reversible lithiation/delithiation process of the LTO/graphene composite. Additionally, 50-LTO-G-600C exhibited a little higher capacity than that of 100-LTO-G-600C due to the larger specific surface area and higher graphene content in the composite. As we expected, the specific capacities were achieved at 140.9 and 158.9 mA h g^{-1} at a current rate of 20 C, respectively. Even at an extremely high current rate of 100 C, the specific capacities of 98.2 and 120.8 mA h g^{-1} (charge/discharge complete within 25 s) could be delivered, corresponding to 56.1% and 70% of the theoretical value, respectively. The outstanding rate capability could be attributed to the synergistic effects of LTO and graphene: the strictly restrained LTO particle size by the ALD seeded route coupled with a hydrothermal reaction as well as low post-sintering temperature (the temperature effect will be discussed in the later part) endowed the LTO with a short lithium ion diffusion path; Meanwhile, graphene as highly conductive framework connected every LTO particle with chemical bond, resulting in an efficiently conductive network for electron and ion transport. The specific capacity of pristine graphene at various current rates derived from charge/discharge potential profiles at the same electrochemical test condition as that of the LTO/graphene composites were also plotted in Fig. S8a in order to quantify each contribution of specific capacity from LTO and graphene in the composite. The specific capacities of 163.5 and 75 mA h g^{-1} were delivered at the first two cycles under the current rate of 0.5 C. After that, reversible capacity was inclined to be stable gradually, proving the SEI formation. However, the specific capacity of graphene was nearly negligible. Fig. S8b shows the contributions of specific capacity from LTO and graphene at various current rates. One can see that LTO contributed to more than 90% total capacity except the initial SEI formation process for both LTO/graphene composites. The contribution ratios of 96.5% and 97.2% at the current rate of 100 C were achieved, corresponding to 50-LTO-G-600C and 100-LTO-G-600C, respectively, demonstrating the capacity output mainly depended on LTO rather than graphene. The dependent relationship of current rates, specific capacity and potential polarization was depicted in Fig. 5c, clearly indicating that 100-LTO-G-600C with smaller potential polarization exhibited better rate performance with the increase of current rate. On the one hand, given that more graphene content (50-LTO-G-600C) is beneficial to improve the rate capability of LTO, on the other hand, more side-effects of SEI (product between graphene and electrolyte) on the electron and ion transport of LTO can not be circumvented after early charge/discharge processes (SEI formation). Additionally, the potential polarization increased for both samples with increasing current rates, which is associated with the increased ohmic and/or diffusion constrains of electrode under high current rates.

The electrochemical kinetics of the LTO/graphene electrode was confirmed by cyclic voltammetry (CV) testing. The corresponding CV curves at various scan rates were shown in Fig. 5d, e. A pair of anodic and cathodic peaks was observed, which is the typical characteristic of the two-phase redox reaction mechanism, consistent with the suggestion of galvanostatic charge/discharge potential profile. The sharp peak with negligible distortion also demonstrated the efficient ion transport of the electrode. The first five CV curves of 50-LTO-G-600C at the scan rate of 0.1 mV s^{-1} were shown in Fig. S9, demonstrating the good reversibility after the initial cycle. The long sloping curve in the initial cycle was associated with the reaction between graphene and electrolyte, consistent with the potential profile. The voltammetric response of the composite electrode at various scan rates obeys a power-law relationship that defines the kinetics mechanism [12,47]. Accordingly, the calculated log(v)-log(i) data based on CV curves was plotted in Fig. 5f. The slopes of 0.57 and 0.61 were obtained (very close to the value of 0.5) corresponding to 50-LTO-G-600C and 100-LTO-G-600C, demonstrating the battery-type diffusion controlled process of the lithation/delithiation rather than the surface control. The cycling rate performance of 50-LTO-G-600C and 100-LTO-G-600C was shown in Fig. 5g. Both samples presented stable reversible capacity even after ultrahigh current rate cycling (100 C). It is worthy of note that 50-LTO-G-600C delivered a little higher capacity at the periods of 0.5 and 1 C (early process) than that of 100-LTO-G-600C owing to the higher surface area and graphene content. However, the capacity was lower than that of 100-LTO-G-600C after 1 C because the side-effects of SEI (reaction between graphene and electrolyte) suppressed its rate capability. We did not define the reaction between graphene and electrolyte as side-reaction since the contribution from graphene host material still existed when the current rate was reset back to 0.5 C. The specific capacities of 184.1 (50-LTO-G-600C) and 191.7 mA h g^{-1} (100-LTO-G-600C) could be restored, which are about 86.5% and 91.5% of the initial values, indicating the high reversibility of composites. The fresh and cycled electrochemical impedance spectroscopy (EIS) of 50-LTO-G-600C and 100-LTO-G-600C were shown in Fig. S10a, b. All the Nyquist plots are composed of a semicircle in a high frequency range and an oblique line in a low frequency range, corresponding to charge transfer resistance (R_{ct}) and lithium ion diffusion into the electrode. The diameter of semicircle represents the R_{ct}, which is generated at the interface between the electrode and electrolyte [48,49]. The fresh 50-LTO-G-600C exhibited a smaller R_{ct} than that of 100-LTO-G-600C due to the high graphene content. After electrochemical cycling, the larger R_{ct} of 50-LTO-G-600C than that of 100-LTO-G-600C could be observed, providing the unequivocal evidence that supports the former explanation of 50-LTO-G-600C with respect to the decreased performance as compared with that of 100-LTO-G-600C. Meanwhile, a new semicircle partially overlapped with R_{ct} was generated and denoted as R_{sei}, corresponding to the resistance of SEI on the surface of electrode [48,49]. 50-LTO-G-600C also exhibited a larger R_{sei} than that of 100-LTO-G-600C, consistent with the former suggestion. The SEM images of cycled 50-LTO-G-600C and 100-LTO-G-600C were characterized in order to give insights into the microstructure especially with respect to SEI as shown in Fig. S11 50-LTO-G-600C with apparently denser SEI morphology could be observed (Fig. S11a, b), furthermore, the corresponding EDS analysis also revealed that elements of C, O, P and Ti are evenly distributed throughout the composite (Fig. S11c, d), consistent with the former explanation as well. The composites exhibited a good cyclic stability of 90% capacity retention at 20 C with nearly 100% Coulombic efficiency after 2500 cycles (Fig. 5h), which is also attributed to the unique structure of LTO and incorporation with efficient graphene host material. Fig. 5i compares the rate capability under various rates and cyclic stability with previous reports (Table S1 (Supporting information) provides the comparison of detailed parameters as well.). The sample in this work surpassed others especially in the extreme high rate and long cycle life metrics, presenting the alluring promise of anode material for EES devices with high power/energy densities.

Additionally, LTO/graphene composites as another control experiment were also synthesized by a hydrothermal method, in which the TiO_2 precursor was prepared by other method rather than this ALD seeding process. The detailed procedure and electrochemical performance (Fig. S12) were described in the Supporting information. The results highlight that this ALD seeding process is crucial to obtain a unique LTO/graphene composite with excellent properties.

The ALD seeded TiO_2 should be hydrothermally lithiated to transform into the LTO precursor. After the post-sintering process at 600 and 800 °C, LTO could be prepared accordingly. The samples were denoted as 100-LTO-G-600C and 100-LTO-G-800C, respectively. The sintering temperature has significant effects on the crystallinity, grain size, defect density, microstructure, furthermore, the electrochemical property. Fig. S13 compares the XRD patterns of 100-LTO-G-600C and 100-LTO-G-800C. The apparently increased intensity of all diffraction peaks of 100-LTO-G-800C was observed. The calculated crystal sizes of 100-LTO-G-600C and 100-LTO-G-800C based on Scherrer equation are ~20 and 50 nm, respectively, demonstrating the high crystallization extent of 100-LTO-G-800C in contrast to 100-LTO-G-600C. Meanwhile, the TEM images also present the morphological difference as shown in Fig. 6a, b. The LTO nanoparticles were still distributed on graphene uniformly. However, some of them merged together, leaving behind large size of nanoclusters (Fig. 6a). The particle diameter distribution was shown in the inset. The calculated average particle size was ~60 nm, which is about three times larger than that of 100-LTO-G-600C. Additionally, the rough surface characteristic was disappeared obviously (Fig. 6b). Fig. S14 presents the nitrogen adsorption/desorption isotherm and the corresponding pore size distribution of 100-LTO-G-800C. The obviously decreased surface area (53.8 m^2 g^{-1}) was obtained as compared with that of 100-LTO-G-600C (126.3 m^2 g^{-1}). The results indicate that low temperature (600 °C) treatment could retard the grain growth and self-merging as well as topological evolution of LTO efficiently. The electrochemical performance was also measured as the control experiment. The cycling rate performance of 100-LTO-G-800C was shown in Fig. 6c. Although the specific capacity was deteriorated as compared with 100-LTO-G-600C, 105.3 and 73.1 mA h g^{-1} at rates of 20 and 100 C were also achieved, respectively. Similarly, 100-LTO-G-800C exhibited a good reversibility as well after high rate cycling. The semicircle of EIS (Fig. 6d) was enlarged apparently, suggesting the increased R_{ct} of electrode. The typical equivalent circuit model was selected as shown in the inset of Fig. 6d. The calculated Rs (corresponds to the equivalent series resistance of the electrode) are 3.2 and 3.6 Ω. And the Rct are 12.5 and 23.5 Ω, corresponding to 100-LTO-G-600C and 100-LTO-G-800C, respectively. The decreased slope of inclined straight line (Warburg impedance) demonstrates the deteriorated ion diffusion into the electrode. The CV curves at various scan rates were plotted in Fig. 6e. The relatively sharp anodic/cathodic peaks with a small distortion were observed. Fig. 6f shows a linear dependence of the anodic peak currents on the square root of scan rate. The slope suggests a diffusion rate of lithium through the solid electrode. As a result, the 100-LTO-G-800C presented a smaller slope, indicating the inferior diffusion rate in contrast to 100-LTO-G-600C. On the one hand, the merged LTO nanoparticles under 800 °C enlarged the lithium ion transport length. On the other hand, it was reported that some kinds of defect structures such as lithium partial occupation and vacancies at the interface of 8a and 16c sites are beneficial for the lithium ion mobility throughout LTO, leading to the high rate capability [50–53]. Therefore, it is established that lithium ion diffused faster along the grain boundary than the diffusion straight through the grain of LTO. It also can be speculated that 100-LTO-G-600C with a low degree of crystallinity provided more grain boundary (defect density), demonstrating the better electrochemical performance accordingly.

First principles calculations were performed on the LTO/graphene composite to better understand excellent electrochemical properties and the effect of different sintering temperatures on LTO. LTO structure was constructed by fixing the $Li_4Ti_5O_{12}$ stoichiometry [54], and geometrical optimization and electronic properties of LTO and LTO/graphene (Fig. 7a–e) were calculated using the projector augmented plane-wave (PAW) method as implemented in the Vienna *ab* Initio Simulation (VASP) program [55]. Perdew-Burke-Ernzerhof (PBE) functional was used with a 500 eV energy cutoff and a *k*-spacing of $2\pi\times0.03$ Å^{-1} for Brillouin zone (BZ) sampling [56]. The calculated electronic structure of defect free LTO (Fig. 7e) shows that the valence states are mainly contributed by O-2*p* and Ti-3*d* states that range from −4.7 to 0 eV below the Fermi level; while the conduction band is dominated by Ti-3*d* states at about 2.6–4.7 eV above the Fermi level. Interestingly, the calculated density of state of the LTO/graphene

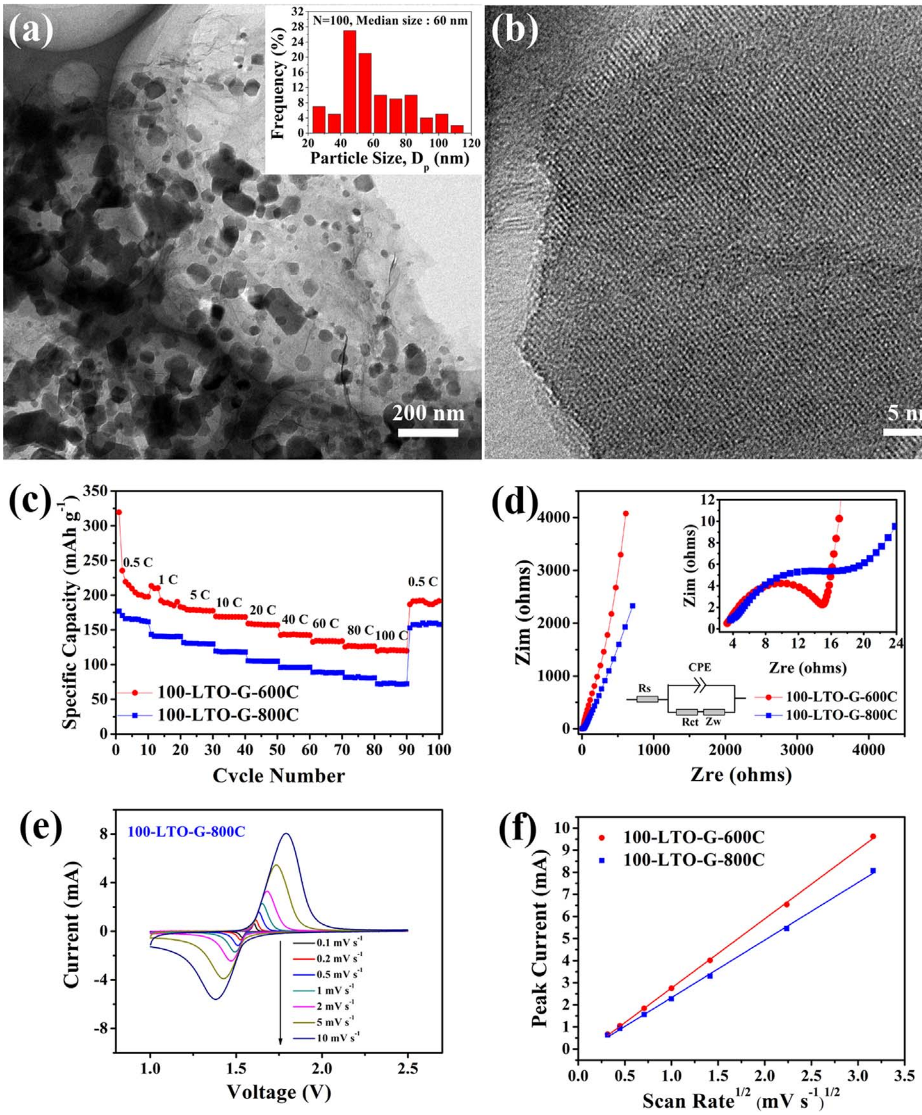

Fig. 6. (a) A bright field TEM image of 100-LTO-G-800C and (inset) the corresponding particle diameter distribution of LTO, (b) a high resolution TEM image of LTO nanoparticles, Comparison of (c) cycling rate performance and (d) EIS of 100-LTO-G-600C and 100-LTO-G-800C, (e) CV curves of 100-LTO-G-800C at various scan rates, and (f) corresponding dependence of peak currents on square root of scan rate as compared with that of 100-LTO-G-600C.

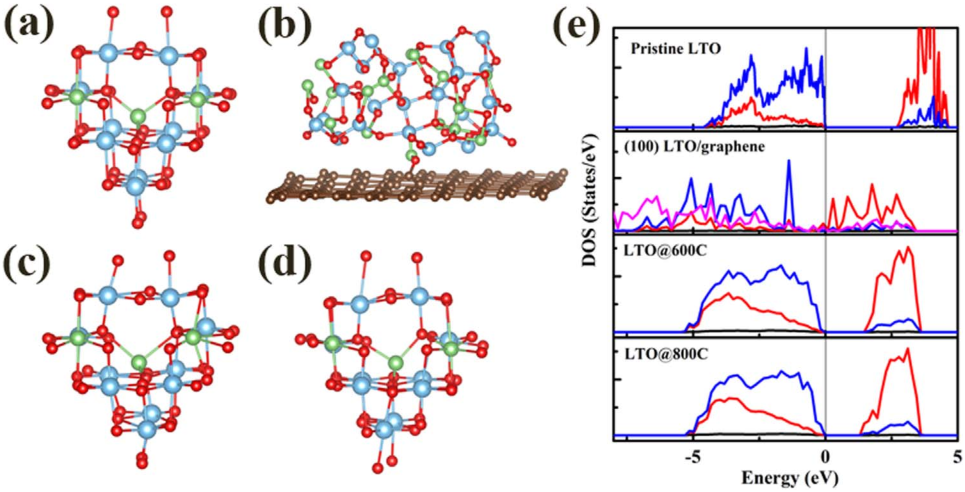

Fig. 7. Selected structural units of original (a) LTO and (b) model of (100) LTO/graphene, LTO units thermal treated at (c) 600 °C and (d) 800 °C, and (e) calculated partial density of states.

composite provides a direct evidence of the electronic conductivity enhancement because of the closure of band gap in contrast to the bare LTO (Fig. 7e), proving the efficient electron and ion transport throughout the LTO/graphene composite. When sintering LTO at 600 and 800 °C, ab initio molecular dynamics simulations (computational method, Supporting information) show that LTO itself shows the semiconducting behavior with a very close band gap of 1.36 and 1.25 eV, respectively. Simultaneously, we found that the coordination number of Li atoms decreases significantly for both LTO samples after heat treatment. Also, 43.3% of Li-O bond distances in the structure at 600 °C is smaller than 1.99 Å of the original structure, in comparison with 40% for the one at 800 °C, which may suggest the shortening of Li diffusion path for the sample of 100-LTO-G-600C [57,58]. Moreover, thermal treatment of LTO under an oxygen-deficient condition may generate oxygen vacancies [59,60]. The calculated density of state for $Li_4Ti_5O_{11.75}$ and $Li_4Ti_5O_{11.5}$ with oxygen vacancies show the modifications of electronic structure from an insulator to a metallic state as demonstrated in Fig. S15, which further supports the improvement of the electronic conductivity [61]. In this regard, 100-LTO-G-600C with more defects may demonstrate a better electrochemical performance as compared with that of 100-LTO-G-800C as well.

In order to further scrutinize the potential of practical applications, the LICs full cell based on the LTO/graphene composite as anode and commercial activated carbon (AC) as cathode was assembled. The corresponding performance was measured and optimized. To obtain the LICs full cell with high energy density, the mass ratio of cathode to anode should be balanced according to the equation of $m_+q_+=m_-q_-$ (q is the specific capacity and m is the mass of active material) due to the asymmetric configuration feature of LICs. The electrochemical property of AC was measured in advanced. The typical specific capacitance of 101 F g^{-1} at the current density of 1 A g^{-1} was selected to match the performance of the LTO/graphene anode (Fig. S16). The LIC full cells with various mass ratios were charged/discharged in the voltage range of 1.5–3.0 V. The obtained energy/power densities with mass ratios from 2.2 to 5.5 (cathode to anode) were shown in the Ragone plots (Fig. 8a). One can see that the energy density was boosted as the mass ratio increased up to 3.5 (the mass of cathode increased); while, the energy density decreased with the further increase of parasitic mass of cathodes, indicating the optimized energy density of the full cell in our experiment. The maximum energy density of 52 W h kg^{-1} at a power density of 225 W kg^{-1} was achieved. The full cell could also deliver an energy density of 35 W h kg^{-1}, which was about 33% energy loss; while, the power density was about 14.4 kW kg^{-1}, which was 64 times larger than the initial value. The maximum power density was 57.6 kW kg^{-1} with a remained energy density of 12.8 Wh kg^{-1}. Such extremely high power density is even better than carbon based symmetric supercapacitor [62–65], proving the outstanding performance of our LTO/graphene composite anode especially under the ultrahigh charge/discharge condition. The comprehensive performance also surpassed reported asymmetric supercapacitors based on LTO and other intercalation type anodes [66–72]. The galvanostatic charge/discharge profiles of the LICs full cell with a mass ratio of 3.5 in the voltage range of 1.5–3.0 V at various current densities was shown in Fig. 8b. The segmented plot with different slopes was obtained. The PF_6^- ions were adsorbed at the interface of AC and electrolyte during the beginning stage of charge process. Meanwhile, the polarized Li^+ ions were intercalated into the LTO/graphene anode to accumulate charges till achieving the capacity balance with AC cathode, demonstrating the integrated mechanisms of SCs and LIBs. The maximum specific capacitance (based on the total mass of active materials) of 55 F g^{-1} at a current density of 0.1 A g^{-1} could be delivered as shown in Fig. 8c. The cyclic performance of LICs full cell was also shown in Fig. 8d, presenting the good capacitance retention of 97% with nearly 100% Coulombic efficiency after 2000 cycles at the current density of 25 A g^{-1}. Only one LICs full cell could power 48 blue light-emitting diodes (LEDs) (1.8 V, 20 mA) as shown in the inset of Fig. 8d, demonstrating the potentially practical application.

4. Conclusion

In summary, we created a novel ALD seeded process coupled with hydrothermal lithiation for synthesis of high performance LTO/graphene composite. TiO_2 nanoislands on graphene as seeds precisely defined by ALD process in advanced ensured the formation of subsequent LTO with unique characteristics. The synergistic effects of nanosized LTO and graphene endow the composite with a short lithium

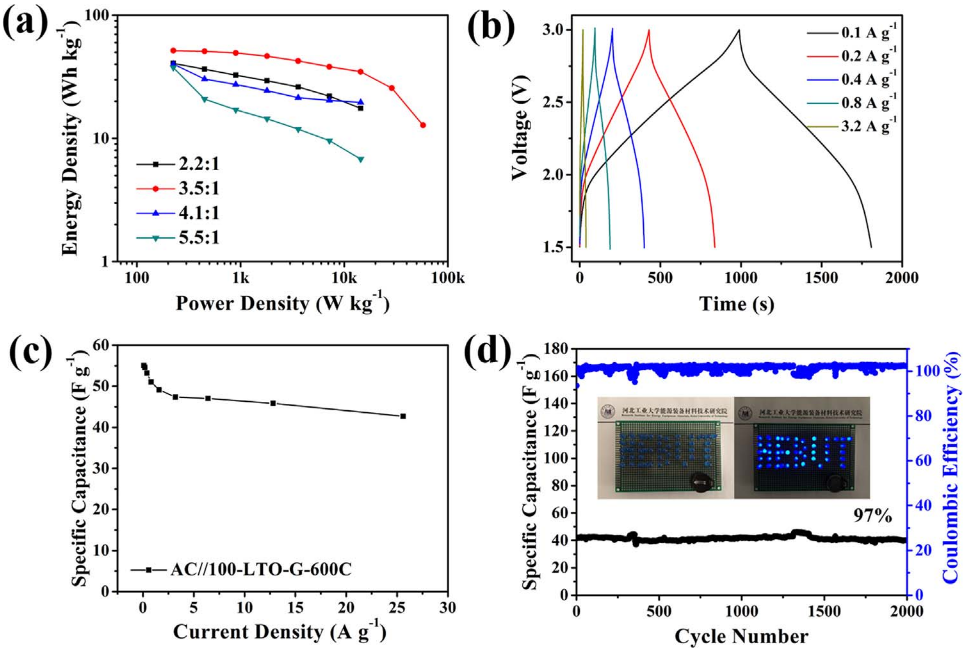

Fig. 8. (a) Ragone plots of LICs full cell based on 100-LTO-G-600C anode and AC cathode under various mass ratios, (b) Galvanostatic charge/discharge profile of LICs full cell with the mass ratio of 4.0, (c) specific capacitance of LICs full cell at various current densities, and (d) cyclic performance of LICs full cell and (inset) digital images of one LICs full cell before and after lighting up 48 blue LEDs.

ion diffusion path and efficiently conductive network for electron and ion transport, boosting the excellent reversible capacity, rate capability, and cyclic stability as anode materials for LICs. Different sintering temperatures after hydrothermal reaction changed the crystallinity, defect density, microstructure as well as the electrochemical property of composite, which were also supported by the theoretical calculation. Our novel route provides a foundation for a feasible design to incorporate energy storage materials onto conductive host materials, propelling the forefront and shedding new light of EES devices with high power/energy densities.

Acknowledgments

The authors gratefully acknowledge the financial support from the National Natural Science Foundation of China (No. 51502073); Natural Science Foundation of Tianjin, China (No. 15JCYBJC53200) and Hebei Province Education Department Science and Technology Research Project (No. QN2015208). J.L acknowledges the financial support from the US National Science Foundation under an award of DMR 1151028. H.G. acknowledges financial support from the National Natural Science Foundation of China (NSFC) under Grants No. 51201148 and U1530402, as well as the Thousand Youth Talents Plan. X.M acknowledges financial support from the National Natural Science Foundation of China (NSFC) under Grants No. 21403188.

Appendix A. Supporting information

Supplementary data associated with this article can be found in the online version at http://dx.doi.org/10.1016/j.nanoen.2017.04.020.

References

[1] S. Chu, A. Majumdar, Nature 488 (2012) 294–303.
[2] M.R. Lukatskaya, B. Dunn, Y. Gogotsi, Nat. Commun. 7 (2016) 12647.
[3] M. Armand, J.M. Tarascon, Nature 451 (2008) 652–657.
[4] N. Nitta, F. Wu, J.T. Lee, G. Yushin, Mater. Today 18 (2015) 252–264.
[5] R. Raccichini, A. Varzi, S. Passerini, B. Scrosati, Nat. Mater. 14 (2015) 271–279.
[6] M.F. El-Kady, Y. Shao, R.B. Kaner, Nat. Rev. Mater. 1 (2016) 16033.
[7] F. Wang, X. Wu, C. Li, Y. Zhu, L. Fu, Y. Wu, X. Liu, Energy Environ. Sci. 9 (2016) 3570–3611.
[8] P. Simon, Y. Gogotsi, Nat. Mater. 7 (2008) 845–854.
[9] K. Naoi, S. Ishimoto, Ji Miyamoto, W. Naoi, Energy Environ. Sci. 5 (2012) 9363–9373.
[10] D.P. Dubal, O. Ayyad, V. Ruiz, P. Gomez-Romero, Chem. Soc. Rev. 44 (2015) 1777–1790.
[11] V. Aravindan, J. Gnanaraj, Y.S. Lee, S. Madhavi, Chem. Rev. 114 (2014) 11619–11635.
[12] V. Augustyn, J. Come, M.A. Lowe, J.W. Kim, P.L. Taberna, S.H. Tolbert, H.D. Abruña, P. Simon, B. Dunn, Nat. Mater. 12 (2013) 518–522.
[13] E. Ferg, R.J. Gummow, A. de Kock, M.M. Thackeray, J. Electrochem. Soc. 141 (1994) L147–L150.
[14] T. Ohzuku, A. Ueda, N. Yamamoto, J. Electrochem. Soc. 142 (1995) 1431–1435.
[15] Y. Sun, L. Zhao, H. Pan, X. Lu, L. Gu, Y.S. Hu, H. Li, M. Armand, Y. Ikuhara, L. Chen, X. Huang, Nat. Commun. 4 (2013) 1870.
[16] C. Wang, S. Wang, L. Tang, Y.B. He, L. Gan, J. Li, H. Du, B. Li, Z. Lin, F. Kang, Nano Energy 21 (2016) 133–144.
[17] H.G. Jung, S.T. Myung, C.S. Yoon, S.B. Son, K.H. Oh, K. Amine, B. Scrosati, Y.K. Sun, Energy Environ. Sci. 4 (2011) 1345–1351.
[18] L. Yu, H.B. Wu, X.W. Lou, Adv. Mater. 25 (2013) 2296–2300.
[19] G.N. Zhu, H.J. Liu, J.H. Zhuang, C.X. Wang, Y.G. Wang, Y.Y. Xia, Energy Environ. Sci. 4 (2011) 4016–4022.
[20] G.N. Zhu, Y.G. Wang, Y.Y. Xia, Energy Environ. Sci. 5 (2012) 6652–6667.
[21] B. Li, C. Han, Y.B. He, C. Yang, H. Du, Q.H. Yang, F. Kang, Energy Environ. Sci. 5 (2012) 9595–9602.
[22] J. Liu, K. Song, P.A. van Aken, J. Maier, Y. Yu, Nano Lett. 14 (2014) 2597–2603.
[23] H. Ni, L.Z. Fan, J. Power Sources 214 (2012) 195–199.
[24] Y. Shi, L. Wen, F. Li, H.M. Cheng, J. Power Sources 196 (2011) 8610–8617.
[25] L. Shen, C. Yuan, H. Luo, X. Zhang, S. Yang, X. Lu, Nanoscale 3 (2011) 572–574.
[26] A.C. Ferrari, F. Bonaccorso, V. Fal'ko, K.S. Novoselov, S. Roche, P. Boggild, S. Borini, F.H.L. Koppens, V. Palermo, N. Pugno, J.A. Garrido, R. Sordan, A. Bianco, L. Ballerini, M. Prato, E. Lidorikis, J. Kivioja, C. Marinelli, T. Ryhanen, A. Morpurgo, J.N. Coleman, V. Nicolosi, L. Colombo, A. Fert, M. Garcia-Hernandez, A. Bachtold, G.F. Schneider, F. Guinea, C. Dekker, M. Barbone, Z. Sun, C. Galiotis, A.N. Grigorenko, G. Konstantatos, A. Kis, M. Katsnelson, L. Vandersypen, A. Loiseau, V. Morandi, D. Neumaier, E. Treossi, V. Pellegrini, M. Polini, A. Tredicucci, G.M. Williams, B. Hee Hong, J.H. Ahn, J. Min Kim, H. Zirath, B.J. van Wees, H. van der Zant, L. Occhipinti, A. Di Matteo, I.A. Kinloch, T. Seyller, E. Quesnel, X. Feng, K. Teo, N. Rupesinghe, P. Hakonen, S.R.T. Neil, Q. Tannock, T. Lofwander, J. Kinaret, Nanoscale 7 (2015) 4598–4810.
[27] K. Chen, S. Song, F. Liu, D. Xue, Chem. Soc. Rev. 44 (2015) 6230–6257.
[28] K.S. Novoselov, V.I. Falko, L. Colombo, P.R. Gellert, M.G. Schwab, K. Kim, Nature 490 (2012) 192–200.
[29] Y. Zhu, S. Murali, W. Cai, X. Li, J.W. Suk, J.R. Potts, R.S. Ruoff, Adv. Mater. 22 (2010) 3906–3924.
[30] K.R. Paton, E. Varrla, C. Backes, R.J. Smith, U. Khan, A. O'Neill, C. Boland, M. Lotya, O.M. Istrate, P. King, T. Higgins, S. Barwich, P. May, P. Puczkarski, I. Ahmed, M. Moebius, H. Pettersson, E. Long, J. Coelho, S.E. O'Brien, E.K. McGuire, B.M. Sanchez, G.S. Duesberg, N. McEvoy, T.J. Pennycook, C. Downing, A. Crossley, V. Nicolosi, J.N. Coleman, Nat. Mater. 13 (2014) 624–630.
[31] X. Xiao, Y. Li, Z. Liu, Nat. Mater. 15 (2016) 697–698.
[32] B. Ahmed, C. Xia, H.N. Alshareef, Nano Today 11 (2016) 250–271.
[33] X. Wang, G. Yushin, Energy Environ. Sci. 8 (2015) 1889–1904.
[34] S.M. George, Chem. Rev. 110 (2010) 111–131.
[35] X. Sun, M. Xie, G. Wang, H. Sun, A.S. Cavanagh, J.J. Travis, S.M. George, J. Lian, J. Electrochem. Soc. 159 (2012) A364–A369.
[36] B. Chunmei, X. Ming, S. Xiang, J.T. Jonathan, W. Gongkai, S. Hongtao, C.D. Anne, L. Jie, M.G. Steven, Nanotechnology 24 (2013) 424002.
[37] G.G. Amatucci, F. Badway, A. Du Pasquier, T. Zheng, J. Electrochem. Soc. 148 (2001) A930–A939.
[38] E. Lim, H. Kim, C. Jo, J. Chun, K. Ku, S. Kim, H.I. Lee, I.S. Nam, S. Yoon, K. Kang, J. Lee, ACS Nano 8 (2014) 8968–8978.
[39] X. Wang, C. Lu, H. Peng, X. Zhang, Z. Wang, G. Wang, J. Power Sources 324 (2016) 188–198.
[40] M. Xiangbo, G. Dongsheng, L. Jian, L. Ruying, S. Xueliang, Nanotechnology 22 (2011) 165602.
[41] I.A. Leonidov, O.N. Leonidova, L.A. Perelyaeva, R.F. Samigullina, S.A. Kovyazina, M.V. Patrakeev, Phys. Solid State 45 (2003) 2183–2188.
[42] Y. Tang, F. Huang, W. Zhao, Z. Liu, D. Wan, J. Mater. Chem. 22 (2012) 11257–11260.
[43] G. Wang, Z. Wang, Z. Liu, J. Xue, G. Xin, Q. Yu, J. Lian, M.Y. Chen, Chem. Eng. J. 260 (2015) 582–589.
[44] S. Stankovich, D.A. Dikin, R.D. Piner, K.A. Kohlhaas, A. Kleinhammes, Y. Jia, Y. Wu, S.T. Nguyen, R.S. Ruoff, Carbon 45 (2007) 1558–1565.
[45] D. Kong, W. Ren, Y. Luo, Y. Yang, C. Cheng, J. Mater. Chem. A 2 (2014) 20221–20230.
[46] K. Zaghib, M. Simoneau, M. Armand, M. Gauthier, J. Power Sources 81–82 (1999) 300–305.
[47] Y. Wang, Z. Hong, M. Wei, Y. Xia, Adv. Funct. Mater. 22 (2012) 5185–5193.
[48] P. Verma, P. Maire, P. Novák, Electrochim. Acta 55 (2010) 6332–6341.
[49] S.S. Zhang, K. Xu, T.R. Jow, Electrochim. Acta 49 (2004) 1057–1061.
[50] M. Wagemaker, D.R. Simon, E.M. Kelder, J. Schoonman, C. Ringpfeil, U. Haake, D. Lützenkirchen-Hecht, R. Frahm, F.M. Mulder, Adv. Mater. 18 (2006) 3169–3173.
[51] M.M. Rahman, J.Z. Wang, M.F. Hassan, D. Wexler, H.K. Liu, Adv. Energy Mater. 1 (2011) 212–220.
[52] W. Schmidt, P. Bottke, M. Sternad, P. Gollob, V. Hennige, M. Wilkening, Chem. Mater. 27 (2015) 1740–1750.
[53] M. Wilkening, R. Amade, W. Iwaniak, P. Heitjans, PCCP 9 (2007) 1239–1246.
[54] K. Kataoka, Y. Takahashi, N. Kijima, J. Akimoto, Ki Ohshima, J. Phys. Chem. Solids 69 (2008) 1454–1456.
[55] G. Kresse, D. Joubert, Phys. Rev. B 59 (1999) 1758–1775.
[56] J.P. Perdew, K. Burke, M. Ernzerhof, Phys. Rev. Lett. 77 (1996) 3865–3868.
[57] J. Jung, M. Cho, M. Zhou, AIP Adv. 4 (2014) 017104.
[58] W.K. Pang, V.K. Peterson, N. Sharma, J.J. Shiu, Sh Wu, Chem. Mater. 26 (2014) 2318–2326.
[59] Y.M. Jiang, K.X. Wang, H.J. Zhang, J.F. Wang, J.S. Chen, Sci. Rep. 3 (2013) 3490.
[60] J.Y. Luo, L.J. Chen, Y.J. Zhao, P. He, Y.Y. Xia, J. Power Sources 194 (2009) 1075–1080.
[61] J.Y. Shin, J.H. Joo, D. Samuelis, J. Maier, Chem. Mater. 24 (2012) 543–551.
[62] X. Fan, C. Yu, J. Yang, Z. Ling, C. Hu, M. Zhang, J. Qiu, Adv. Energy Mater. 5 (2015) (1401761-n/a).
[63] J. Zhao, H. Lai, Z. Lyu, Y. Jiang, K. Xie, X. Wang, Q. Wu, L. Yang, Z. Jin, Y. Ma, J. Liu, Z. Hu, Adv. Mater. 27 (2015) 3541–3545.
[64] T. Lin, I.W. Chen, F. Liu, C. Yang, H. Bi, F. Xu, F. Huang, Science 350 (2015) 1508–1513.
[65] C. Chen, D. Yu, G. Zhao, B. Du, W. Tang, L. Sun, Y. Sun, F. Besenbacher, M. Yu, Nano Energy 27 (2016) 377–389.
[66] H. Xu, X. Hu, Y. Sun, W. Luo, C. Chen, Y. Liu, Y. Huang, Nano Energy 10 (2014) 163–171.
[67] D. Puthusseri, V. Aravindan, B. Anothumakkool, S. Kurungot, S. Madhavi, S. Ogale, Small 10 (2014) 4395–4402.
[68] Q. Wang, Z.H. Wen, J.H. Li, Adv. Funct. Mater. 16 (2006) 2141–2146.
[69] T. Zhang, F. Zhang, L. Zhang, Y. Lu, Y. Zhang, X. Yang, Y. Ma, Y. Huang, Carbon 92 (2015) 106–118.
[70] A. Jain, V. Aravindan, S. Jayaraman, P.S. Kumar, R. Balasubramanian, S. Ramakrishna, S. Madhavi, M.P. Srinivasan, Sci. Rep. 3 (2013) 3002.
[71] R. Gokhale, V. Aravindan, P. Yadav, S. Jain, D. Phase, S. Madhavi, S. Ogale, Carbon 80 (2014) 462–471.
[72] K. Leng, F. Zhang, L. Zhang, T. Zhang, Y. Wu, Y. Lu, Y. Huang, Y. Chen, Nano Res. 6 (2013) 581–592.

Gongkai Wang received his Ph.D. degree in Materials Science and Engineering from Northeastern University, China in 2012. He is currently an assistant professor in Research Institute for Energy Equipment Materials, Hebei University of Technology. His research interests mainly focus on nanostructured materials for energy storage and thermal management applications.

Chengxing Lu obtained his Bachelor's degree in Materials science and Engineering from Inner Mongol University of Technology in 2014. He is now a graduate student at School of Materials science and Engineering, Hebei University of Technology, supervised by Prof. Xin Wang and Dr. Gongkai Wang. His research focuses on the synthesis of nanomaterials and their applications in energy storage.

Xin Zhang received her Ph.D. degree in Materials Science and Engineering from Northeastern University, China in 2013. She is currently an assistant professor in Research Institute for Energy Equipment Materials, Hebei University of Technology. Her research interests mainly focus on microscopic characterizations of multifunctional materials.

Biao Wan received his master degree in Materials Science and Engineering from Yanshan University in 2015. Currently, he is a joint Ph.D. in Center for High Pressure Science and Technology Advanced Research (HPSTAR). His current research focuses on the theoretical prediction and experimental research of new functional materials.

Hanyu Liu received his Ph.D. in Condensed Matter Physics, State Key Lab of Superhard materials, Jilin University in 2013. Now, he is a postdoctoral research associate at Geophysical Lab, Carnegie Institution of Washington, USA. Hanyu is interested in studying superconductivity in light elements at high pressures and the properties of materials at extreme conditions using molecular dynamics and crystal structure predictions.

Meirong Xia received her Ph.D. in Chemical engineering and technology from the Chongqing University, Chongqing, China, in 2013. Afterwards she worked as a lecturer at the Yanshan University. Her research interests include the theoretical calculations and experiments for development of electrochemical catalysts with high activity, long-term stability for PEM fuel cell, electrochemical capacitors, metal-air fuel cell and nanocarbon materials. Dr Xia has published more than 30 peer-reviewed papers. She also held patents on novel catalysts for hydrogen evolution electrode.

Huiyang Gou received his Ph.D. degree in Materials Science and Engineering from Yanshan University in 2009. Currently, he is staff scientist at Center for High Pressure Science and Technology Advanced Research (HPSTAR). His research focuses on the theoretical and experimental understanding novel materials under ambient and extreme conditions, in particular, superhard, superconducting and energy-based materials.

Guoqing Xin obtained his Ph.D. degree in Mechanical Engineering from Rensselaer Polytechnic Institute in 2016. He is currently a postdoc research associate in Rensselaer Polytechnic Institute. His research focuses on graphene fibers and batteries.

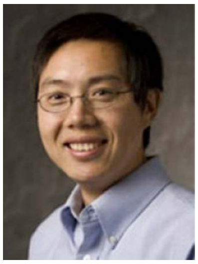

Jie Lian received his Ph.D. degree in Nuclear Engineering & Radiological Sciences from University of Michigan in 2003. He is currently an associate professor in Department of Mechanical, Aerospace & Nuclear Engineering, Rensselaer Polytechnic Institute. His research interests include materials behavior under extreme conditions, materials with enhanced performance for advanced nuclear systems and nanostructured materials for alternative energy applications.

Yongguang Zhang is an Associate Professor of Research Institute for Energy Equipment Materials at Hebei University of Technology, China. He received his BS degree in chemical engineering from Tianjin University, and earned his Ph.D. in chemical engineering at University of Waterloo in 2013. His current interests include the synthesis and characterization of nanomaterials for energy storage and conversion, especially for lithium-ion batteries and lithium/sulfur batteries.